RSC Advances

PAPER

View Article Online
View Journal | View Issue

Cite this: *RSC Adv.*, 2026, **16**, 5490

Influence of CeO_2-doped glass powder on silver paste performance in photovoltaic solar cells

Wang Donghui,[a] Gan Guoyou,*[a] Tang Xianjie,[a] Yu Xianglei,[a] Li Junpeng,[b] Wan Ruixi[a] and Yang Tao[a]

Received 20th October 2025
Accepted 20th January 2026

DOI: 10.1039/d5ra08036c

rsc.li/rsc-advances

With the advancement of green photovoltaic solar cells, silver paste has sparked vast research interest. As a key functional component of silver paste, glass powder plays a vital role by etching the SiN_x layer to achieve ohmic contact with the silicon layer. To investigate the influence of individual oxides on the Te–Bi–B glass system, this study doped 0.5 wt% CeO_2, ZrO_2, and Nb_2O_5 into the Te–Bi–B system and prepared a series of glass powders *via* the high-temperature quenching method. The effects of these dopants on key parameters, including high-temperature flowability, wettability, and thermal stability, were systematically investigated. The results indicate that all three glass powders exhibit suitable glass transition temperatures but undergo relatively pronounced crystallisation reactions. Among them, the CeO_2-doped glass powder demonstrates superior chemical stability, high-temperature flowability, and wettability. Therefore, CeO_2 is identified as the optimal dopant oxide, and silver paste prepared from it significantly enhanced Ag–Si interface bonding, achieving maximum silver electrode adhesion (3.87 N) and minimum volume resistivity (2.8×10^{-8} Ω m), thereby demonstrating excellent sintering performance. Furthermore, the CeO_2-doped glass powder significantly influences the etching of silicon emitters and the Ag–Si ohmic contact structure, reducing contact resistance in photovoltaic solar cells and consequently improving their photovoltaic conversion efficiency (23.17%).

1. Introduction

In recent years, the issue of energy shortages has become increasingly severe, highlighting the pressing need for the development of renewable energy sources. Photovoltaic power generation has experienced rapid development, driven by its outstanding advantages of sustainability, environmental cleanliness, and geographical flexibility. Concurrently, market demand has propelled photovoltaic solar cells toward reduced cost and enhanced efficiency, carrying significant implications for foundational materials such as silver paste.[1–4] The front-side silver paste plays a pivotal role as a key material in the fabrication of electrodes for crystalline silicon solar cells. Its performance directly affects several parameters of solar cells, including series resistance (R_s), short-circuit current (I_{sc}), fill factor (FF), and photoelectric conversion efficiency (η).[5–9] As the binder phase in silver paste, glass powder can etch through the SiN_x layer on the cell surface, enabling Ag–Si ohmic contact, promoting fusion and densification of silver particles, and forming electrodes with excellent conductivity and adhesion. The performance of glass powder directly influences the sintering properties and interfacial current transport of silver paste, ultimately affecting the photovoltaic conversion efficiency of the solar cell.[10–17]

Research on glass powders for silver paste applications has advanced significantly, primarily encompassing Pb-, Te-, Bi-based, and multi-component lead-free systems. While traditional lead-based systems offer excellent performance, they are gradually being phased out due to advances in green technology.[18,19] Among various oxides, Bi_2O_3 is recognised as an environmentally friendly material, meeting green environmental standards. In glass powders, PbO and Bi_2O_3 exhibit comparable physical and chemical properties.[14,20–23] Meanwhile, the incorporation of TeO_2 enhances the reaction activity and high-temperature fluidity.[24] Therefore, Bi_2O_3 and TeO_2 are often employed as substitutes for PbO and have consequently become the focus of glass powder research. Currently, Te- and Bi-based glasses have been extensively investigated and widely applied. Sun *et al.* investigated lead-free Bi_2O_3–TeO_2 glass powders with optimized TeO_2 content to achieve superior high-temperature flowability and wettability. However, increasing TeO_2 content in the glass reduces its ability to dissolve and precipitate silver, thereby diminishing the current transport efficiency of the Ag–Si interface glass layer.[25] Fu *et al.* investigated silver paste prepared from Bi_2O_3–B_2O_3–ZnO glass systems, which exhibited excellent adhesion and a dense microstructure on $MgTiO_3$ substrates. This material has been applied in high-performance power electronic device packaging.[26] However, the

[a]*Faculty of Materials Science and Engineering, Kunming University of Science and Technology, Kunming 650093, Yunnan, China. E-mail: ganguoyou@kust.edu.cn*
[b]*Kunming Institute of Precious Metal, Kunming 650093, Yunnan, China*

comprehensive properties of Te- and Bi-based glass systems, particularly their influence on Ag–Si contact structures and the sintering performance of silver pastes,[27] still require further systematic investigation and optimization.

To elucidate the mechanisms by which different components influence the properties of the Te–Bi–B glass system, three functional metal oxides (CeO_2, ZrO_2, and Nb_2O_5) were chosen for single-variable doping studies. Each of the three materials possesses distinct physical and chemical properties within the glass structure. CeO_2 may act as a network modifier, wherein Ce^{4+} exhibits strong oxidising properties. During high-temperature sintering, it undergoes redox reactions with Si and N in the SiN_x layer, locally and controllably etching the silicon nitride layer. This process creates pathways for silver–silicon contact, facilitating the formation of high-quality ohmic interfaces. ZrO_2 can serve as a network intermediate, markedly enhancing the chemical stability of the glass. In addition, Nb_2O_5 may act as a network-forming agent, thereby improving its electrical properties. We analyze the independent mechanisms of action of these three oxides with distinct properties within the Te–Bi–B glass system by introducing them while keeping other components constant. Our study reveals the specific effects of the aforementioned dopants on glass properties, adhesion strengths, the formation of silver microcrystals and nanoparticles at the Ag–Si interface, as well as their etching reactions. Furthermore, we establish a clear "composition–structure–property" relationship and identify the optimal dopant oxide that can enhance glass properties, providing valuable insight for the development of next-generation, high-performance, environmentally benign, lead-free glass powders for silver paste.

2. Experimental

2.1 Experimental materials

This study employed semi-finished n-type monocrystalline silicon solar cells of industrial-grade M10 size (182 mm × 182 mm) with a resistivity of 1–3 Ω cm, which had undergone surface texturing processing. The glass powder was primarily composed of Bi_2O_3 (99.5%, Zhengzhou PainI), TeO_2 (99.0%, Tianjin Yaohua), B_2O_3 (99.5%, Tianjin Fuchen), ZnO (≥99.7%, Aladdin Reagent), NaF (≥99.0%, Aladdin Reagent), and Li_2O (≥99.0%, Aladdin Reagent), with dopants (CeO_2 (≥99.0%, Aladdin Reagent), ZrO_2 (≥99.0%, Aladdin Reagent), and Nb_2O_5 (≥99.0%, Aladdin Reagent)) added separately during preparation. The organic carrier was prepared using ethyl cellulose (Aladdin), diethylene glycol dibutyl ether (98%, Aladdin), and rosin alcohol (98%, Aladdin). Silver powder was procured from China Platinum Metals Co., Ltd. The screen-printing stencils were supplied by Kunshan Screen Printing Products Co., Ltd.

2.2 Preparation of glass powder

The glass powders were prepared using the high-temperature melting method. The oxides were accurately weighed in the specific proportions using an electronic balance. The thoroughly mixed oxides were ground in a mortar, and the blended mixture was transferred to an alumina crucible, which was placed into the muffle furnace for heating at 1200 °C. The heating rate was set to 10 °C min^{-1} and the temperature was held at 1200 °C for half an hour. Half of the molten glass was rapidly poured into deionized water for quenching, causing abrupt cooling and solidification into fine glass particles. The other half was poured into a 5 × 5 × 25 mm mold (using boron nitride as a release agent) and cooled naturally. Further, these glass particles were kept in a drying oven for 24 h. After drying, the dried glass particles were mixed with ethanol and subjected to wet ball milling at 300 rpm for 20 h. Finally, the glass powder was sieved through a 400-mesh screen to obtain the desired particle size. The prepared glass powder samples were labelled as A1, A2, and A3 according to the different dopants added (Table 1).

2.3 Preparation of glass powder pellets

The glass powder tablets were prepared using a cylindrical tableting die (dimensions: 5 mm, model: HF-5, depth: 20 mm, material: CR12). A total of 0.5 g of glass powder was weighed and mixed with anhydrous ethanol in a 90 wt% : 10 wt% ratio to form a uniform paste with optimal viscosity and dispersion. The mixed samples were evenly distributed between the two gaskets inside the cylindrical mold cavity. The press rod was then inserted and gently rotated to flatten the samples, preventing uneven pressure and protecting the mold walls. The assembled mold was placed at the center of the tableting workbench. After tightening the tableting screws, 0.1 MPa of pressure was applied to the sample for 60 s. The resulting cylindrical samples (diameter: 5 mm, height: 6 mm) were removed from the mold and placed on a Si wafer. Finally, the samples were heated in a muffle furnace at 400 °C, 500 °C, 600 °C, 650 °C, 700 °C, and 800 °C for 90 s each.

2.4 Preparation of silver electrodes

The silver powder, organic carrier, and glass powder were accurately weighed in a ratio of 83 wt% : 15 wt% : 2 wt% using an electronic balance. The mixture was ground evenly in an agate mortar and rolled into a slurry using a three-roll mill. The fineness of the silver paste was tested with a scraper fineness tester, and rolling was continued until the fineness of the silver paste was less than 10 μm. Silver paste containing different glass powders was prepared and screen-printed onto silicon wafers. The printed wafers were allowed to level for 10 min, then dried in a constant-temperature oven at 160 °C for 20 min. Finally, the wafers were sintered in a chain-type infrared furnace for 90 s at a maximum temperature of 820 °C to obtain silver electrodes. The resulting electrodes prepared with different oxide dopants were labeled as PA1, PA2, and PA3.

Table 1 Composition ratios of three glass powder samples

Sample	Bi_2O_3	TeO_2	B_2O_3	CeO_2	ZrO_2	Nb_2O_5	ZnO	NaF	Li_2O
A1	55	14.5	15	0.5	0	0	10	2	3
A2	55	14.5	15	0	0.5	0	10	2	3
A3	55	14.5	15	0	0	0.5	10	2	3

2.5 Preparation of test samples

The silver paste was printed onto silicon wafers according to patterns for volume resistivity testing and adhesion testing, followed by sintering. The silver layer pattern for the volume resistivity test consisted of two silver wires of 15 mm × 2 mm, while the pattern for adhesion testing consisted of 10 mm × 10 mm squares. The sintered solar cell was cut perpendicular to the silver electrode to obtain longitudinal cross-section samples. The solar cell sample was immersed in HNO_3 for 8 min at 60 °C to etch away the silver layer from the silver electrode, exposing the glass layer. Subsequently, the sample with the exposed glass layer was dipped in 5 mol per L HF (10 min) for a second etching step to remove the glass layer and any silver particles dispersed within it, thereby exposing the Si layer.

2.6 Characterization methods and performance testing

Using a thermogravimetric-differential scanning calorimeter (TG-DSC, Q2000, TA Corporation), the glass powder was heated to 900 °C in a nitrogen atmosphere to test its thermal stability. The amorphous state and crystallisation of the glass powder were characterized using X-ray diffractometer (XRD, D8-Advance, Germany). Using a thermomechanical analyzer (TA TMA Q400, USA), the glass was heated at a rate of 5 °C min^{-1} to 300 °C. The linear thermal expansion coefficient (CTE) in the thickness direction of the glass was measured in compression mode, and the compatibility between the glass and the single-crystal silicon wafer was evaluated. The contact angle measuring instrument (SL200KS, Kino Industries, USA) was used to observe the morphological changes of glass laminates with increasing temperature and to measure the contact angle. Further, the cross-sectional morphology of the solar cell samples and the surface microstructures of the glass and Si layers were examined using a scanning electron microscope (SEM, Hitachi SU8010, Hitachi Instruments). The sheet resistance of the silver electrodes was determined using a four-probe resistance tester (ST-2258C, Suzhou Lattice Electronics Co., Ltd, China), and the corresponding volume resistivity was calculated. Adhesion strength of the silver electrodes was measured using a digital push–pull gauge with a range of 10 N. Electrical performance testing of solar cells with printed silver electrodes was evaluated using a Halm tester. The particle size of the glass powder samples was analyzed by using a laser particle size analyzer (Dandong Baiter Instrument Co., Ltd).

3. Results and discussion

To evaluate the thermal properties of the glass powders, differential scanning calorimetry test was performed on the

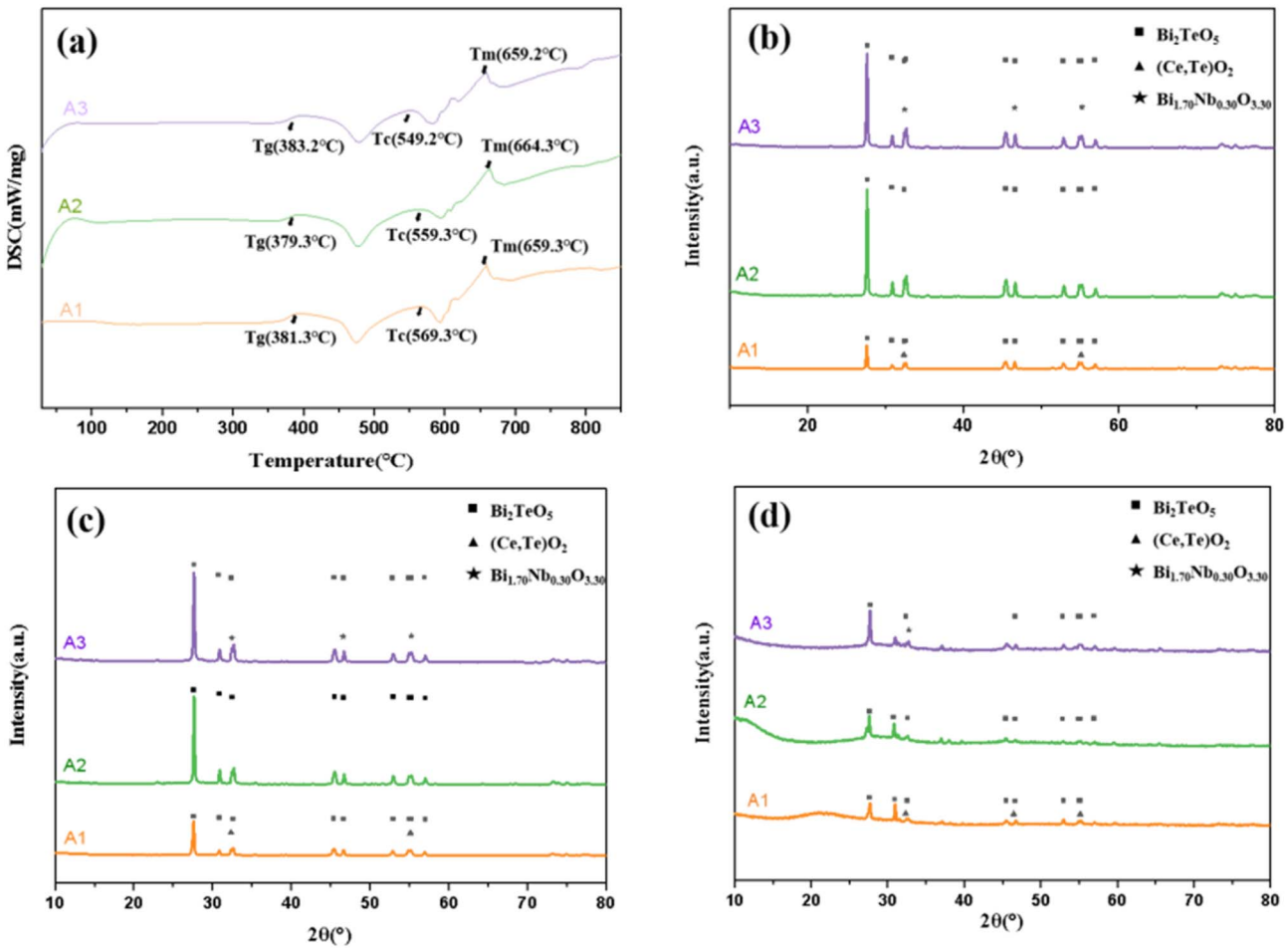

Fig. 1 Characterization of glass powder sample: (a) DSC curve; (b–d) XRD patterns after heating to 580 °C, 650 °C, and 800 °C, respectively.

samples. As shown in Fig. 1a, the glass transition temperature (T_g), glass crystallisation temperature (T_c), and glass melting onset temperature (T_m) were determined for glass powder samples A1, A2, and A3. The corresponding temperature differences, ΔT ($T_c - T_g$) for A1, A2, and A3 are 188 °C, 180 °C, and 167 °C, respectively. The glass transition temperature ranges from a maximum of 383.2 °C to a minimum of 379.3 °C. The T_g values of the three glass samples are relatively low and exhibit only minor variation, which facilitates softening during the initial stages of sintering and promotes silver dissolution. Each sample (A1, A2, and A3) exhibits a crystallisation peak around 470 °C, followed by a melting peak near 580 °C. Beyond 600 °C, minor crystallisation and melting peaks appear, and the glass begins to melt above 650 °C. The parameter ΔT represents the chemical stability of the glass powders, indicating that A1 exhibits the highest chemical stability, while A3 demonstrates the lowest. The DSC curve shows that after the T_g, the crystallisation and melting peaks of A1 are more gradual than those of A3. A1 exhibits better chemical stability, corresponding to the maximum ΔT value of A1.

For the XRD analysis, A1, A2, and A3 sample tablets were placed on silicon wafers and heated at 580 °C, 650 °C, and 800 °C, respectively, for 1 min, followed by cooling to room temperature. The XRD results confirm the phase transitions occurring during the crystallisation of glass powders as shown in the DSC curves (Fig. 1b–d). Sharp diffraction peaks are observed at 580 °C for glass powders A1, A2, and A3 (Fig. 1b). Comparison with the PDF standard patterns indicates that these peaks correspond to the Bi_2TeO_5 phase, which represents a low-energy, highly stable crystal structure in the Te–Bi phase diagram.

Simultaneously, A1 exhibits CeO_2 and TeO_2 diffraction peaks, where the crystalline phases containing Ce and Te significantly attenuate the intensity of the Bi_2TeO_5 diffraction peaks. In contrast, A3 shows a $Bi_{1.70}Nb_{0.30}O_{3.30}$ diffraction peak, corresponding to the crystalline phase of Nb and Bi. Compared with A2, the $Bi_{1.70}Nb_{0.30}O_{3.30}$ phase causes a slight decrease in the intensity of the Bi_2TeO_5 diffraction peak; however, this reduction is far less pronounced than the attenuation observed when CeO_2 and TeO_2 interact with Bi_2TeO_5. As shown in Fig. 1c,

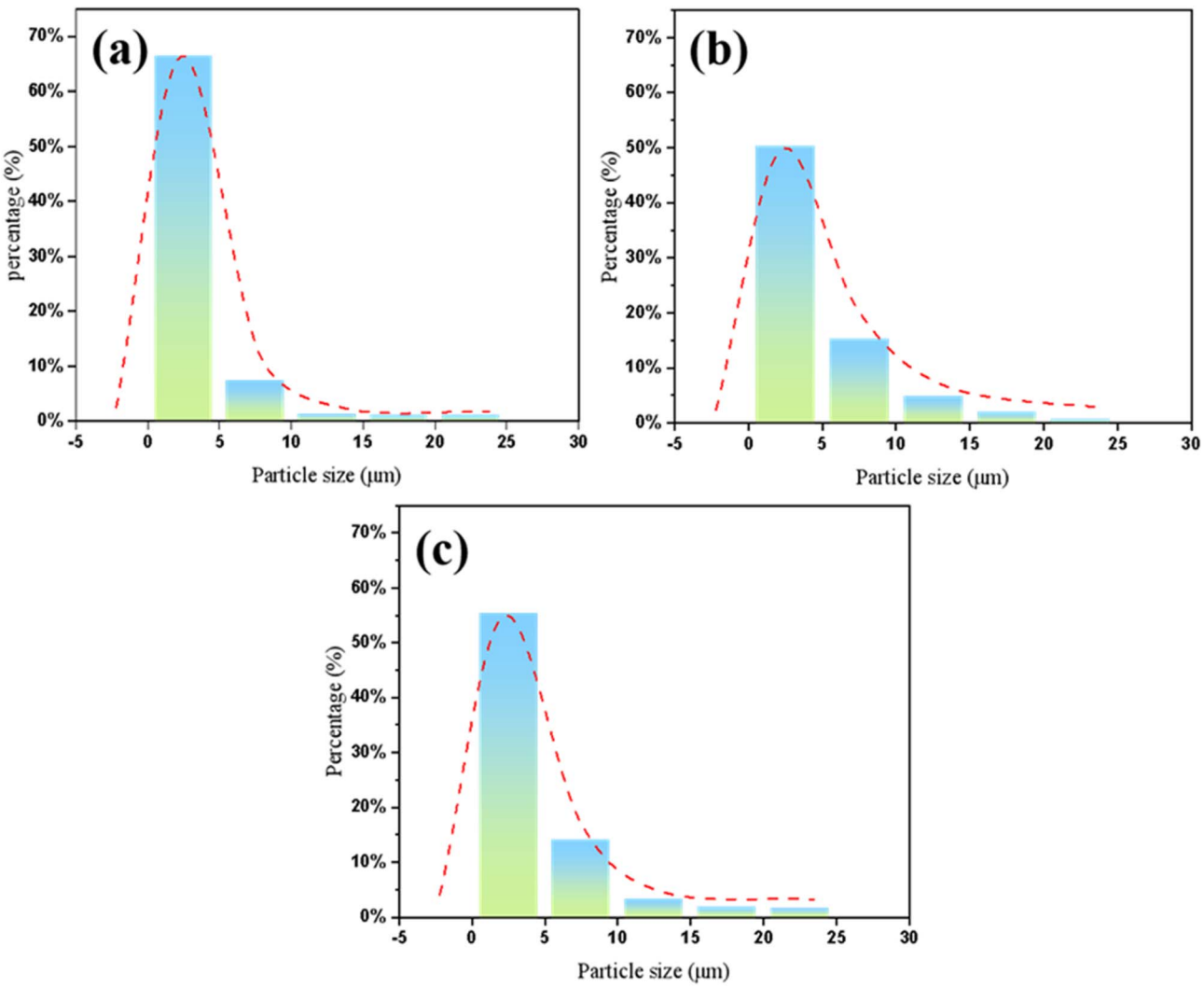

Fig. 2 Particle size distribution: (a) glass powder A1; (b) glass powder A2; (c) glass powder A3.

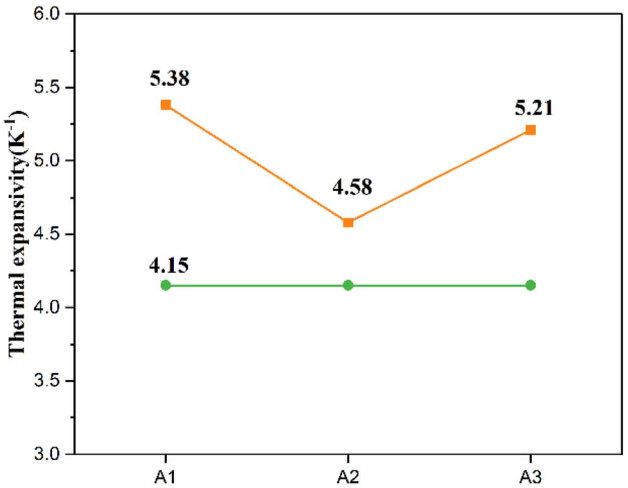

Fig. 3 Thermal expansion coefficient curves of glass powders A1, A2, and A3.

the intensities of the Bi_2TeO_5 diffraction peaks simultaneously decrease when glass powders A1, A2, and A3 are heated at 650 °C. In addition, the peak positions shift slightly to higher angles, indicating a weakened crystallisation reaction in the glass powders. This demonstrates that, with increasing temperature, the crystalline phase gradually diminishes, transitioning toward an amorphous state. The diffraction peaks of the Ce- and Te-containing crystalline phases, together with those of $Bi_{1.70}Nb_{0.30}O_{3.30}$ continuously affect the intensity of the Bi_2TeO_5 diffraction peak, thereby influencing the precipitation of the Bi_2TeO_5 phase. At 800 °C, the diffraction peak intensities of A1, A2, and A3 decrease significantly, along with the appearance of an amorphous peak. This indicates that at 800 °C, the glass powder predominantly exists in an amorphous state, with only minor diffraction peaks corresponding to the Bi_2TeO_5, CeO_2, TeO_2, and $Bi_{1.70}Nb_{0.30}O_{3.30}$ phases being observed. Since the actual cooling rate during silver paste sintering is comparable to or faster than the natural cooling rate of the glass powders after heating, the glass state after heating at 800 °C closely resembles that of the glass phase following silver paste sintering. Consequently, the glass phase in silver pastes prepared from the three types of glass powders remains predominantly amorphous after sintering. Fig. 1d shows that the number of Bi_2TeO_5 diffraction peaks in the three glass powders follows the order A2 > A3 > A1. Among the three samples, A2 consistently exhibits greater precipitation of Bi_2TeO_5 crystals. Although the $Bi_{1.70}Nb_{0.30}O_{3.30}$ phase in A3 suppresses Bi_2TeO_5 precipitation, the Bi_2TeO_5 diffraction peak intensity remains consistently higher than that of A1. While crystalline phases disappear after glass melting and do not reprecipitate during cooling, they delay the softening and flow process of the glass. Overall, glass powder A1 offers the best thermal stability performance.

The particle size distribution of the ball-milled glass powders was analyzed using a laser particle size analyzer, as shown in Fig. 2a–c. The particle size distributions of glass powders A1, A2, and A3 were similar. The median particle sizes (D50) of samples A1, A2, and A3 were 2.481 μm, 4.933 μm, and 4.204 μm, respectively, which are close to the particle size of the silver powder used in the experiment. The specific surface areas were 1493 $m^2\ kg^{-1}$, 914.3 $m^2\ kg^{-1}$, and 990.5 $m^2\ kg^{-1}$, respectively. It can be observed that smaller powder particles exhibit a larger specific surface area and higher surface activation energy. During the sintering process, the finer glass powder disperses well within the silver powder, enabling close contact between silver particles and promoting sintering behavior. Consequently, it is inferred that glass powder A1 exhibits the best sintering performance.

Fig. 3 shows the thermal expansion coefficients of naturally cooled glass powder samples after TMA testing. During the test, we obtained the functional relationship between the sample's thickness dimension and temperature variation. The thermal expansion coefficients of glass powders A1, A2, and A3 were calculated using the formula $\alpha(T) = (\Delta L/L_0)/\Delta T$. The empirical formula for the thermal expansion coefficient $\alpha(T)$ of monocrystalline silicon is:

$$\alpha(T) = A + B \times T + C \times T^2 + D \times T^3 \quad A = -2.885 \times 10^{-7}$$
$$B = 4.910 \times 10^{-9} \quad C = -2.765 \times 10^{-12}$$
$$D = 5.982 \times 10^{-16}$$

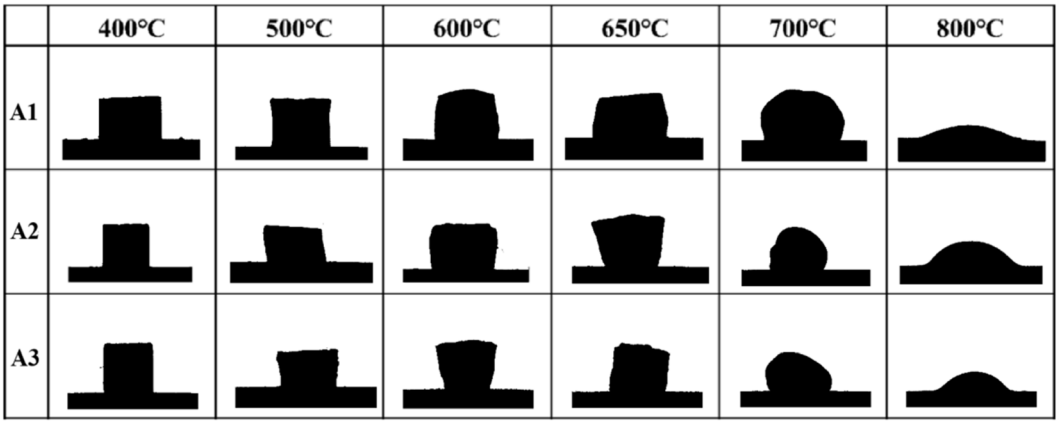

Fig. 4 Morphological changes observed in glass powders A1, A2, and A3 after heating from 400 °C to 800 °C.

The yellow curve in the figure represents the thermal expansion coefficients of three glass powder samples, which are 5.38 ppm K^{-1}, 4.58 ppm K^{-1}, and 5.21 ppm K^{-1}, respectively; the green curve represents the thermal expansion coefficient of monocrystalline silicon (4.15 ppm K^{-1}). During silver paste sintering, the expansion and contraction of the glass phase must align as closely as possible with the silicon wafer. The degree of thermal expansion coefficient matching between the glass phase and the silicon wafer determines the adhesion of the silver layer after sintering. Severe mismatch between the two may lead to issues such as shrinkage at the silver paste interface, surface cracking, and reduced adhesion. The thermal expansion coefficients of glass powders A1, A2, and A3 follow the order A1 > A3 > A2. Their respective differences from the silicon substrate are 1.23 ppm K^{-1}, 0.43 ppm K^{-1}, and 1.06 ppm K^{-1}. All three samples exhibit thermal expansion coefficients slightly higher than monocrystalline silicon, indicating excellent compatibility with silicon wafers.

Further, the morphological variation of the glass powders was investigated by placing the prepared sample pellets on 20 mm × 20 mm Si wafers and heating them at 400 °C, 500 °C, 600 °C, 650 °C, 700 °C, and 800 °C for 1 min each. As shown in Fig. 4, the morphology of the sample remains virtually unchanged at 400 °C. However, as the temperature gradually approaches the glass softening point, the glass enters a highly viscoelastic state, generating internal contraction stresses that cause the sample to shrink in volume. When the temperature exceeds 600 °C, the glass powder reaches its initial crystallisation temperature. During this stage, nucleation and crystal growth lead to volume expansion, resulting in spheroidization during the initial melting phase. As the temperature increases further, melting becomes more complete, and under the influence of gravity, the glass samples then diffuse toward the surface of the Si wafer. At 700 °C, A3 exhibits a higher degree of melting, whereas at 800 °C, only sample A1 spreads completely across the silicon wafer surface, thus demonstrating the best flowability among all samples. Fig. 5a–c presents the contact angles of the samples A1, A2, and A3 with Si wafers at 800 °C, which follow the trend A2 > A3 > A1. The glass melt derived from glass powder A1 exhibits superior high-temperature wettability on the silicon wafer surface. The DSC results were further validated by characterizing the morphological changes of the glass powder during sintering at different temperatures, confirming that glass powder A1 possesses enhanced sintering performance.

Silver paste prepared from different glass powders was printed onto Si wafers using various test patterns and sintered at a peak temperature of 820 °C. The influence of different oxide additives in glass powders A1, A2, and A3 on the sintering performance of the silver pastes was evaluated by analyzing their volume resistivity and adhesion after sintering (Fig. 6). As shown in Fig. 6a, the average adhesion values of the silver electrodes PA1, PA2, and PA3 are 3.87 N, 2.42 N, and 3.15 N, respectively, indicating substantial variation in adhesion strength. The standard deviations of adhesion are 0.32, 0.17, and 0.40. Further, Fig. 6b presents the average volume resistivities of the three silver electrodes as 2.8×10^{-8} Ω m, 4.07×10^{-8} Ω m, and 3.29×10^{-8} Ω m, respectively. The standard deviations of the volume resistivity are 0.28, 0.33, and 0.18. These findings indicate that the adhesion strength of the silver electrodes after sintering is inversely proportional to their volume resistivity. Among the samples, the silver electrode PA1 exhibits the best overall sintering performance, and doping with CeO_2 enhances the sintering properties of the silver paste.

By examining the microstructure of the silver electrode cross-sections and analysing the surface changes in the glass layer and silicon wafer, variations in adhesion and volume resistivity were evaluated. The relationship between the glass powder and the sintering properties of the silver paste was investigated. Fig. 7 presents SEM images of the cross-sectional and etched surface morphologies of the silver electrodes. In Fig. 7a–c, the glass layer is observed to sink during the silver paste sintering process, forming a "pathway" between the silver layer and the silicon emitter. White silver nanoparticles of varying sizes and shapes are dispersed throughout the glass layer, and their distribution changes significantly with variations in the glass powder composition. This occurs because, during glass melting, the silver powder in the paste exhibits differing abilities to dissolve and precipitate silver particles within the glass layer. Depending on the different oxides added to the glass powder, the glass layer thickness follows the order PA1 > PA3 > PA2. In the PA1 silver electrode, the glass layer thickness exceeds the height of the pyramid structure on the cell surface. Glass powder A1 in PA1 exhibits excellent high-temperature flowability. During sintering, the glass powder melts and flows through the gaps between silver particles, reaching the Ag–Si interface and thereby increasing the effective contact area. Simultaneously, the glass undergoes interfacial reactions with the silicon emitter surface, resulting in high bonding strength. Consequently, the silver electrode PA1 demonstrates the highest adhesion. Although the glass layer thickness of the silver electrode PA3 decreases after sintering, it can still form a continuous glass layer between the silver layer and the silicon

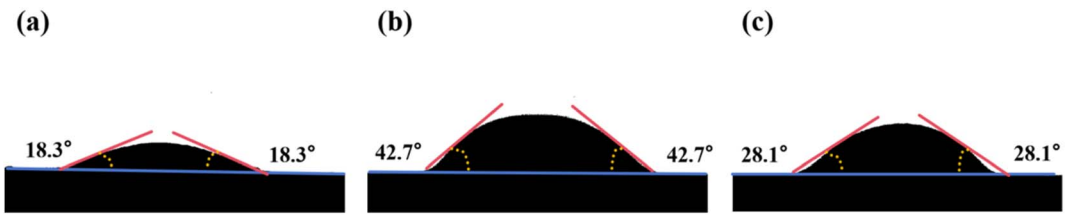

Fig. 5 The contact angle when heated to 800 °C: (a) glass powder A1; (b) glass powder A2; (c) glass powder A3.

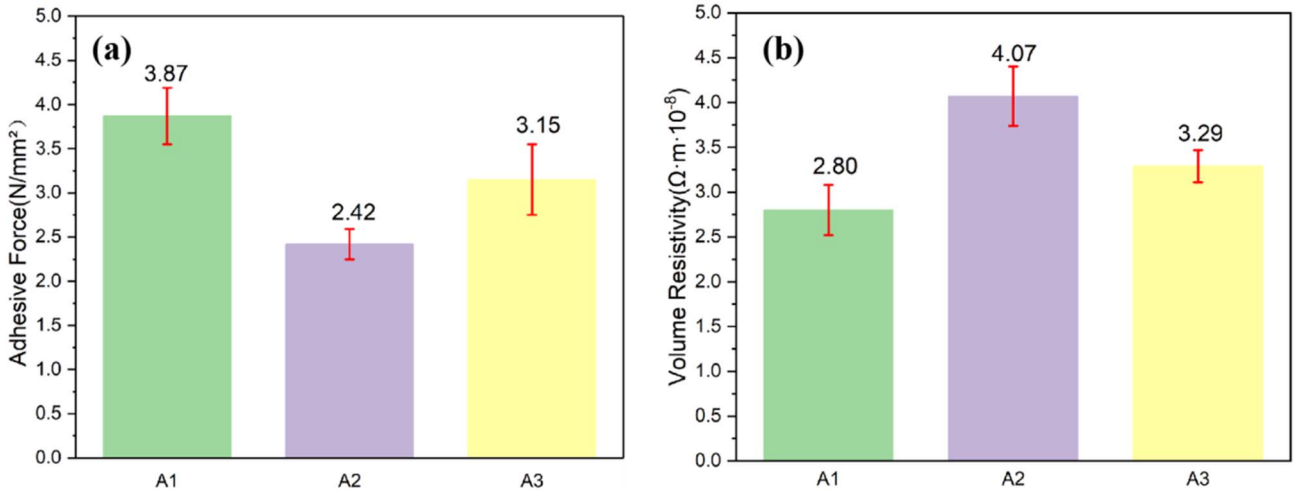

Fig. 6 (a) Adhesive force of glass powders A1, A2, and A3; (b) their volume resistivity.

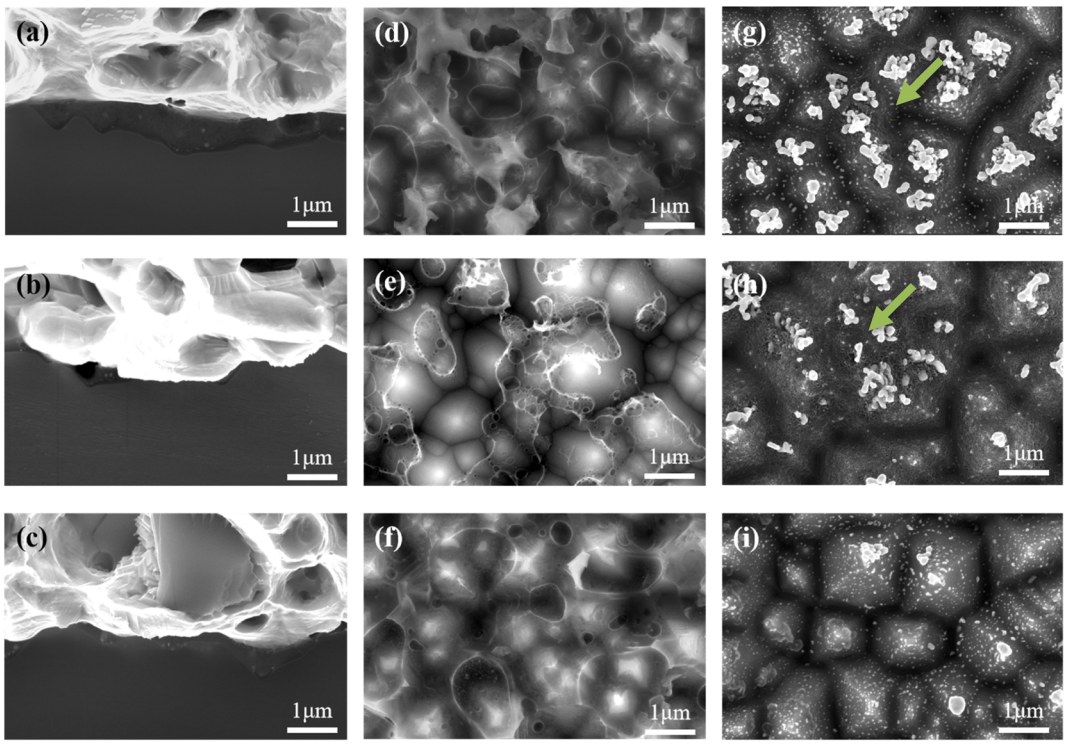

Fig. 7 SEM images of silver electrodes PA1, PA2, and PA3: (a–c) cross-sectional images; (d–f) glass layer surface after HNO_3 etching. (g–i) SEM images of the silicon emitter surface after HNO_3 and HF etching of silver electrode PA1, PA2, and PA3, respectively.

emitter. Therefore, its adhesion is slightly lower than that of PA1. However, in most regions of PA2, the silver layer directly contacts the silicon emitter surface, resulting in a pronounced reduction in glass layer thickness. This weakens the Ag–Si interface reaction and lowers the bonding strength, leading to a marked decrease in the adhesion of the silver electrode PA2. Fig. 7d–f show SEM images of the glass layer after the silver layer was etched away using HNO_3. As shown in Fig. 7d, the glass layer of PA1 extensively covers the pyramidal structure on the silicon surface. The layer is relatively thick and non-uniform, exhibiting protrusions with sharp edges. This can be attributed to the underside of the silver layer in contact with the glass layer developing an uneven surface during the sintering of fine particles, with the silver particles exhibiting limited fusion and growth. In Fig. 7e, the glass layer on the silver electrode PA2 exhibits a mesh-like structure dispersed across the silicon emitter surface. The limited coverage of the glass layer exposes the pyramidal texture of the silicon layer, indicating that only a small amount of glass has flowed to the Ag–Si interface. This finding aligns with the cross-sectional morphology of the silver

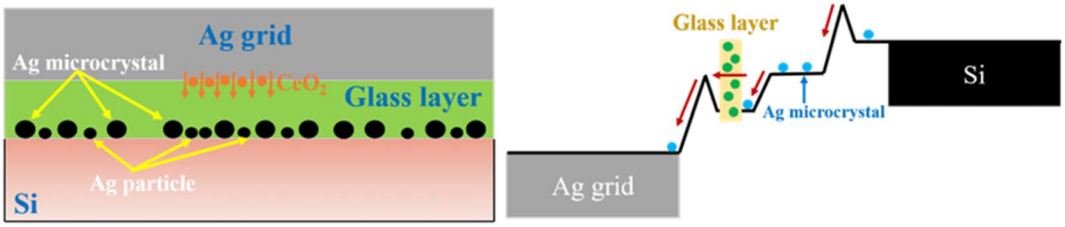

Fig. 8 Formation of silver electrodes and interface transfer process in photovoltaic solar cells.

electrode depicted in Fig. 7b. Furthermore, although the glass layer on the silver electrode PA3 extensively covers the silicon layer's pyramidal structure, the underlying morphology remains discernible (Fig. 7f). The glass layer contains numerous silver nanoparticles and exhibits a relatively smooth surface. This indicates that the glass exhibits strong silver dissolution and precipitation abilities, resulting in increased particle size at the base of the silver layer and a relatively smoother surface. SEM images obtained after further removal of the glass layer are shown in Fig. 7g–i. The glass and silver layers were removed from the silver electrode PA1 (Fig. 7g). Fine etching pits appeared on the surface of the pyramid structure, indicating a slight etching reaction between the glass powder (A1) in the silver paste and the silicon layer. It prevents the pyramid structure of the silicon layer from being damaged, as indicated by the green arrow. The Si layer is coated with numerous silver nanoparticles (10–100 nm) and silver microcrystals larger than 100 nm.[28] Among these, silver nanoparticles are primarily concentrated in the voids at the base of the pyramid structures and within the etched pits on their surfaces. At the apex of the pyramids, irregularly shaped and agglomerated silver microcrystals are densely distributed. In Fig. 7h, the number of silver nanoparticles is significantly decreased, with only a small amount adhering to the etched pits on the pyramid surfaces. The observations reveal that the etched pits on the pyramid surface have deepened, causing extensive damage to the pyramid morphology. This suggests that the etching reaction between the silver paste and the silicon layer has intensified. In contrast, Ce etching of SiN_x layers is efficient and controllable. In Fig. 7i, the silver electrode PA3 exhibits a high density of silver nanoparticles, with clear evidence of particle growth. The pyramidal structures remain intact, and the surface etching pits are noticeably reduced. However, silver microcrystals are distributed only at the tips of individual pyramidal structures. Overall, increasing the Ce content in the glass enhances its ability to dissolve and precipitate silver, effectively corroding the SiN_x layer, leading to a higher number of silver nanoparticles within the glass, thereby promoting the growth of silver microcrystals on the surface of the silicon emitter. Nb facilitates the growth of both silver nanoparticles and silver microcrystals; however, it also intensifies the etching reaction on the SiN_x layer. For optimal electrical contact, the glass layer must etch the SiN_x layer without causing structural damage, while the silver nanoparticles in the glass layer help to reduce its electrical resistance. Simultaneously, the silver nanocrystals grown on the silicon surface act as conductive pathways, reducing the contact resistance between the silver layer and the solar cell.[29] Consequently, the volume resistivity of the silver electrode PA1 is lower than that of PA2 and PA3.

To better understand the mechanism of CeO_2 during the sintering process of silver electrodes, Fig. 8 illustrates the formation of the silver electrode and the interfacial transport process. As shown in the figure, when CeO_2 is doped, the high-temperature fluidity and stability of the glass are optimized. During sintering, CeO_2 precipitates downward, forming a stable structure with the Ag layer and the silicon emitter. Numerous silver nanoparticles and silver microcrystals deposit on the surface of the silicon emitter, as indicated by the yellow arrows. In the interfacial transport process, the silver microcrystals effectively reduce the potential barrier for electron transport, while the silver nanoparticles within the glass layer ensure smooth electron conduction through the glass layer, thereby enhancing the electron transport efficiency at the Ag–Si interface.

To compare the electrical performance of interface current transport, *I–V* performance tests were conducted on the silicon wafers of PA1, PA2, and PA3 using a Halm tester (Table 2). As shown in the table, the series resistance (R_s) of silver electrode PA1 is the lowest, while its short-circuit current (I_{sc}) is the highest. The large number of silver microcrystals grown on the printed silver electrode PA1 of the solar cell provides ample conductive pathways at the Ag–Si interface, and the low volume resistivity leads to reduced contact resistance. In addition, the silver electrode PA1 exhibits strong etching capability on the solar cell without damaging the silicon emitter structure, resulting in low parallel resistance (R_{sh}) and a reduced open-circuit voltage (V_{oc}). Although the silicon wafer with the printed silver electrode PA2 exhibits a large number of silver microcrystals, this severely compromises the structure of the silicon emitter. Consequently, its series resistance (R_s) is higher than that of PA3, while the short-circuit current (I_{sc}) is lower. Furthermore, due to the differences in conversion efficiencies (η) among the three silver electrodes, as shown in Fig. 9, PA1 exhibits the highest η, followed by PA3, with PA2 having the

Table 2 *I–V* performance testing of three silver electrodes

Sample	I_{sc} (A)	V_{oc} (V)	R_s (mΩ)	R_{sh} (Ω)	FF (%)	η (%)
PA1	13.71	0.6853	1.29	839	81.57	23.17
PA2	13.48	0.6877	1.55	845	81.61	23.03
PA3	13.63	0.6904	1.43	858	81.60	23.14

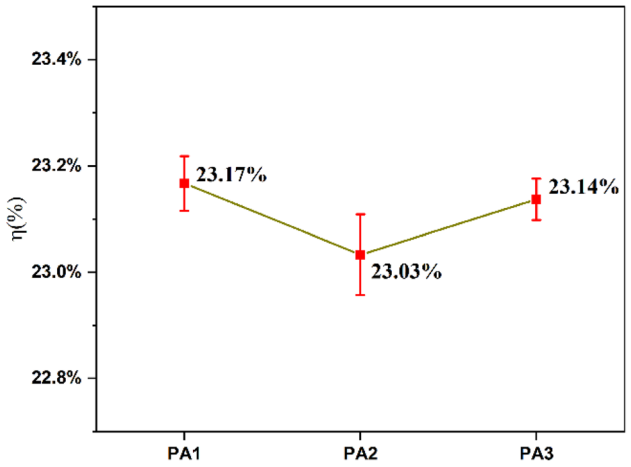

Fig. 9 Photoelectric conversion efficiencies of silver electrodes PA1, PA2, and PA3.

lowest. In summary, the solar cell printed with the PA1 silver electrode demonstrates the best performance.

Based on the finding that 0.5% CeO_2 doping enhances the adhesion and electrical properties of silver paste, glass powders with CeO_2 doping concentrations of 0%, 0.25%, and 0.75% (designated as A4, A5, and A6, respectively) were further prepared. These powders were used to fabricate corresponding silver electrodes labeled PA4, PA5, and PA6. In total, four glass powder samples (including the previously studied 0.5% doped variant) and four silver electrodes were prepared with a doping concentration gradient of 0.25%.

The influence of CeO_2 doping concentration on the Ag–Si interface and the severity of silicon etching was investigated by analyzing the cross-sectional microstructure of the silver electrodes and the etching of the silicon wafer by the glass layer. As shown in Fig. 10a–d, the glass layer in the undoped electrode (PA4) exhibits uniform thickness. Within the region marked by

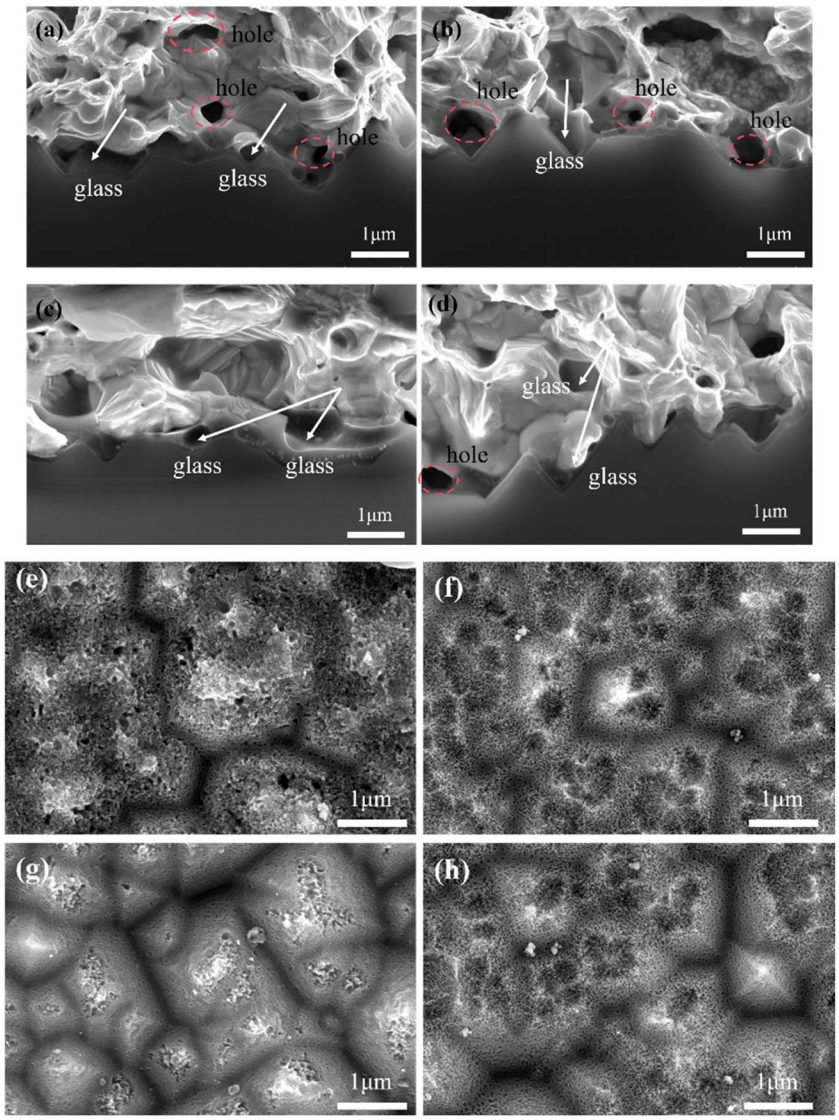

Fig. 10 (a–d) Cross-sectional SEM images of silver electrodes PA4, PA5, PA1, and PA6. (e–h) SEM images of silicon wafer surfaces after removal of silver microcrystals and silver particles from silver electrodes PA4, PA5, PA1, and PA6.

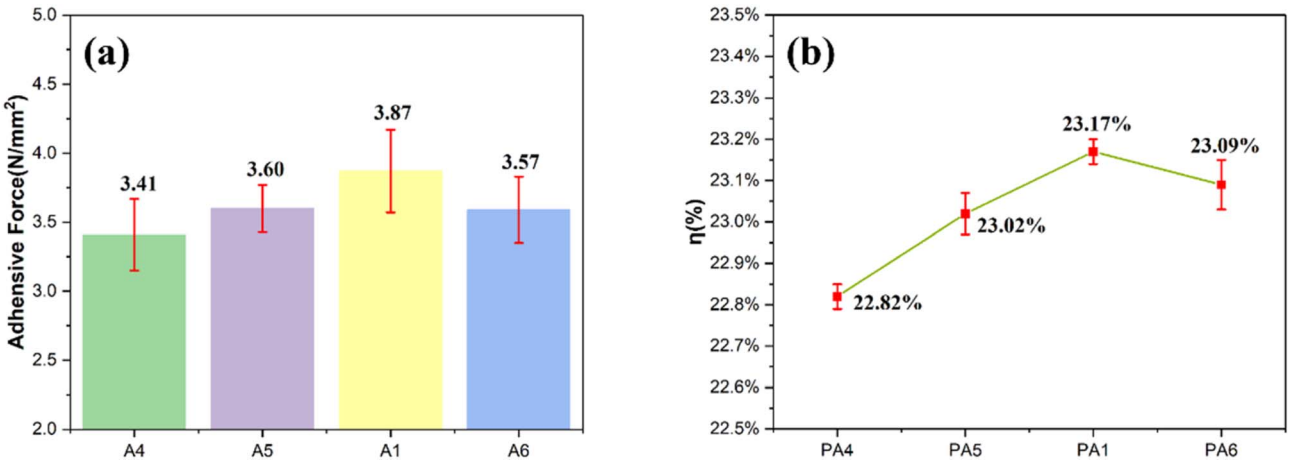

Fig. 11 (a) Adhesion of silver electrodes PA4, PA5, PA1, PA6. (b) Photovoltaic conversion efficiency of silver electrodes PA4, PA5, PA1, PA6.

the red dashed line, relatively large pores are present. Silver nanoparticles, mostly under 100 nm in size, are formed within the glass layer and deposited onto the surface of the silicon emitter, with very few silver microcrystals observed. At 0.25% CeO_2 doping, pores remain near the glass layer, and no significant microstructural changes are evident compared to the undoped sample. When the doping concentration reaches 0.5%, the silver particles in electrode PA1 increase in size and distribute uniformly throughout the glass layer, accompanied by the disappearance of pores. However, at a higher doping concentration of 0.75%, less glass flows onto the silicon wafer (as indicated by the white arrows), leaving residual glass within the silver layer. Additionally, a small number of pores reappear under this condition. Fig. 10e–h illustrate that the extent of silicon wafer etching first decreased and then increased with rising CeO_2 doping concentration. In the absence of CeO_2 doping, the silicon surface underwent severe etching, which destroyed the pyramidal texture. At a doping concentration of 0.5%, the pyramidal structure of the silicon wafer remained largely intact, with only the tips showing slight etching.

Silver pastes were prepared by screen-printing glass and silver powders with varying doping concentrations, followed by sintering at 820 °C for 60 s. The adhesion strength and photovoltaic conversion efficiency of the resulting silver electrodes (designated PA4, PA5, PA1, and PA6) were subsequently evaluated. As shown in Fig. 11a, the average adhesion values of the four electrodes were 3.41 N, 3.60 N, 3.87 N, and 3.57 N, respectively. The overall variation in adhesion was relatively limited, which can be attributed to the consistent thickness of the glass layer. Nevertheless, voids present within the silver layer were found to modify the interfacial reaction with the silicon emitter surface, thereby influencing the resultant bond strength. The photovoltaic conversion efficiencies of the electrodes are presented in Fig. 11b. Across the series, efficiency first increased and then decreased, reaching an optimum at a dopant concentration of 0.5%. The presence of pores and the extent of glass-induced etching of the silicon wafer were identified as key factors affecting the photoconversion performance. To enhance efficiency, it is essential to minimize pore formation, ensure etching of the SiN_x layer without damaging the p–n junction. In summary, silver electrodes fabricated using glass powder doped with 0.5% CeO_2 exhibited the highest adhesion strength and the best photovoltaic conversion efficiency among the investigated samples.

4. Conclusion

Various glass powders were prepared by doping Te–Bi–B glass powders with CeO_2, ZrO_2, and Nb_2O_5, while keeping the other components constant. Silver paste was prepared by uniformly mixing the glass powder, silver powder, and an organic binder, followed by screen printing to form silver electrodes. Characterization of the glass powders and silver electrodes revealed the following:

(1) The CeO_2-doped glass powder exhibited an appropriate glass transition temperature. During crystallization, the Ce- and Te-containing crystalline phases significantly suppressed the precipitation of the Bi_2TeO_5 phase. Under high-temperature conditions, the CeO_2-doped glass powder spread completely over the silicon wafer, showing the smallest contact angle. Consequently, this glass powder demonstrated the best high-temperature wettability and flowability.

(2) When the CeO_2-doped glass powder was used to fabricate silver electrodes, a uniform and continuous glass layer formed at the Ag–Si interface. This glass layer completely covered the silicon emitter surface, enhancing its strength. Within the Ag–Si contact structure, the glass layer effectively etched the SiN_x anti-reflective layer without damaging the pn junction. This facilitated the growth of silver nanoparticles and deposition on the silver microcrystalline silicon surface. Adhesion, volume resistivity, and electrical properties were evaluated for PA1, PA2, and PA3. When doped with CeO_2, adhesion reached 3.87 N, volume resistivity was 2.8×10^{-8} Ω m, and the photovoltaic conversion efficiency achieved 23.17%.

In addition, long-term aging experiment is an important indicator for the industrialization of photovoltaic solar cells. Based on the current research, we will develop appropriate durability tests to obtain more complete data.

Conflicts of interest

There are no conflicts to declare.

Data availability

The authors declare that the data supporting the findings of this study are available within the paper. Should any raw data files be needed in another format they are available from the corresponding author upon a reasonable request.

Acknowledgements

This work has been awarded the Major Science and Technology Projects in Yunnan Province [No. 202402AB080005]; The Science and Technology projects of Yunnan Precious Metals Laboratory [No. YPML-2023050206 and YPML-20240502102].

References

1 H. E. Çiftpınar, M. K. Stodolny, Y. Wu, G. J. M. Janssen, J. Löffler, J. Schmitz, M. Lenes, J.-M. Luchies and L. J. Geerligs, *Energy Procedia*, 2017, **124**, 851–861.
2 F. Haase, C. Hollemann, S. Schäfer, A. Merkle, M. Rienäcker, J. Krügener, R. Brendel and R. Peibst, *Sol. Energy Mater. Sol. Cells*, 2018, **186**, 184–193.
3 B. Kafle, B. S. Goraya, S. Mack, F. Feldmann, S. Nold and J. Rentsch, *Sol. Energy Mater. Sol. Cells*, 2021, **227**, 111100.
4 C. Ballif, F.-J. Haug, M. Boccard, P. J. Verlinden and G. Hahn, *Nat. Rev. Mater.*, 2022, **7**, 926.
5 K. T. Butler, P. E. Vullum, A. M. Muggerud, E. Cabrera and J. H. Harding, *Phys. Rev. B:Condens. Matter Mater. Phys.*, 2011, **83**, 235307.
6 A. Chaudhary, J. Hoß, J. Lossen, F. Huster, R. Kopecek, R. Van Swaaij and M. Zeman, *Phys. Status Solidi A*, 2021, **218**, 2100243.
7 M. A. Green, E. D. Dunlop, M. Yoshita, N. Kopidakis, K. Bothe, G. Siefer and X. Hao, *Progress in Photovoltaics: Research and Applications*, 2023, vol. 31, pp. 651–663.
8 S. Seyedmohammadi, E. Graddy and A. Shaikh, in *2010 35th IEEE Photovoltaic Specialists Conference*, IEEE, Honolulu, HI, USA, 2010, pp. 003600–003603.
9 B. Gerdes, M. Jehle, N. Lass, L. Riegger, A. Spribille, M. Linse, F. Clement, R. Zengerle and P. Koltay, *Sol. Energy Mater. Sol. Cells*, 2018, **180**, 83–90.
10 L. Mo, L. Zhao, C. Zhou, G. Wang and W. Wang, *Mater. Lett.*, 2022, **324**, 132752.
11 B. Feng, Y. Liu, W. Chen, G. Xing, X. Chen and X. Du, *Sol. Energy Mater. Sol. Cells*, 2023, **257**, 112381.
12 J. Zhang, J. Zhou, J. Huang and B. Lv, *Sol. Energy Mater. Sol. Cells*, 2022, **238**, 111585.
13 P. Kumar, Z. Aabdin, M. Pfeffer and O. Eibl, *Sol. Energy Mater. Sol. Cells*, 2018, **178**, 52–64.
14 Y.-S. Lai, S.-S. Lai, Y.-J. Li, H.-J. Lin and T.-H. Chiang, *J. Alloys Compd.*, 2021, **858**, 157646.
15 X.-X. Pi, X.-H. Cao, J.-S. Chen, L. Zhang, Z.-X. Fu, L.-X. Wang and Q.-T. Zhang, *Rare Met.*, 2021, **40**, 84–89.
16 X. Sun, S. Yao, J. Xing, J. Zhang, Y. Yang, H. Li, H. Tong and X. Yuan, *Mater. Res. Express*, 2020, **7**, 016315.
17 S. Watanabe, T. Kodera and T. Ogihara, *J. Ceram. Soc. Jpn.*, 2015, **123**, 345–350.
18 S. Chen, C. Guo, J. Feng, X. Zhang, R. An, Z. Liu, H. Du, Y. Gou, C. Xiao, W. Liu, J. Yang, M. Xu, Y. Tan, Z. Gu, Y. Qiao, C. Li, Z. Yang, Y. Zeng, W. Zhang and J. Ye, *Small Methods*, 2025, **9**, 2401753.
19 X.-X. Pi, X.-H. Cao, J.-S. Chen, L. Zhang, Z.-X. Fu, L.-X. Wang and Q.-T. Zhang, *Rare Met.*, 2021, **40**, 84–89.
20 J.-T. Tsai, L.-K. Lin, S.-T. Lin, L. Stanciu and M. B.-G. Jun, *Mater. Des.*, 2021, **200**, 109453.
21 D. S. Jung, J. H. Kim, Y. J. Hong and Y. C. Kang, *Electron. Mater. Lett.*, 2012, **8**, 643–648.
22 W. Yang, Q. Sun, Q. Lei, W. Zhu, Y. Li, J. Wei and M. Li, *J. Mater. Process. Technol.*, 2019, **267**, 61–67.
23 X. Zhang, Y. Zhang, C. Wang, P. Zhu, B. Xiang, T. Zhao, L. Xu and R. Sun, in *2022 23rd International Conference on Electronic Packaging Technology (ICEPT)*, IEEE, Dalian, China, 2022, pp. 1–6.
24 A. N. D'Souza, *Mater. Chem. Phys.*, 2023, **293**(126657).
25 H. Sun, X. Yu, S. Quan, W. Li, Z. Qian, J. Li and G. Gan, *RSC Adv.*, 2024, **14**, 6048–6057.
26 Y. Fu, X. Yu, L. Liu, X. Tang, J. Li and G. Gan, *Micromachines*, 2023, **14**, 1663.
27 S. Yao, J. Xing, J. Zhang, S. Xiong, Y. Yang, X. Yuan, H. Li and H. Tong, *J. Mater. Sci.:Mater. Electron.*, 2018, **29**, 18540–18546.
28 W. Oh, J. Park, S. Dimitrijev, E. K. Kim, Y. S. Park and J. Lee, *Sol. Energy*, 2020, **195**, 527–535.
29 X. Yu, W. Li, H. Sun, Z. Qian, J. Li, Y. Yu and G. Gan, *Front. Mater.*, 2024, **11**, 1359856.